Inorganic Chemistry

pubs.acs.org/IC

Article

# Quantifying Variations in Metal–Ligand Cooperative Binding Strength with Cyclic Voltammetry and Redox-Active Ligands

Kyle D. Spielvogel,[§] Nathan C. Stumme,[§] Taylor V. Fetrow, Li Wang, Javier A. Luna, Jason M. Keith,* Scott K. Shaw,* and Scott R. Daly*

Cite This: *Inorg. Chem.* 2022, 61, 2391–2401

Read Online

ACCESS | Metrics & More | Article Recommendations | Supporting Information

**ABSTRACT:** Metal–ligand cooperativity (MLC), a phenomenon that leverages reactive ligands to promote synergistic reactions with metals, has proven to be a powerful approach to achieving new and unprecedented chemical transformations with metal complexes. While many examples of MLC are known with a wide range of substrates, experimentally quantifying how ligand modifications affect MLC binding strength remains a challenge. Here we describe how cyclic voltammetry (CV) was used to quantify differences in MLC binding strength in a series of square-pyramidal Ru complexes. This method relies on using multifunctional ligands (those capable of both MLC and ligand-centered redox activity) as electrochemical reporters of MLC binding strength. The synthesis and characterization of Ru complexes with three different redox-active tetradentate ligands and two different ancillary phosphines ($PPh_3$ and $PCy_3$) are described. Titration CV studies conducted using $BH_3$·THF with $BH_3$ as a model MLC substrate allowed $\Delta G_{MLC}$ to be quantified for each complex. Compared to our base triaryl ligand, increasing $\pi$ conjugation in the backbone of the redox-active ligand enhanced MLC binding, whereas increasing $\pi$ conjugation in the flanking groups decreased the MLC binding strength. Structures and spectroscopic data collected for the isolated MLC complexes are also described along with supporting DFT calculations that were used to illuminate electronic factors that likely account for the observed differences in the MLC binding strength. These results demonstrate how redox-active ligands and CV can be used to quantify subtle differences in the MLC binding strength across a series of structurally related complexes with different ligand modifications.

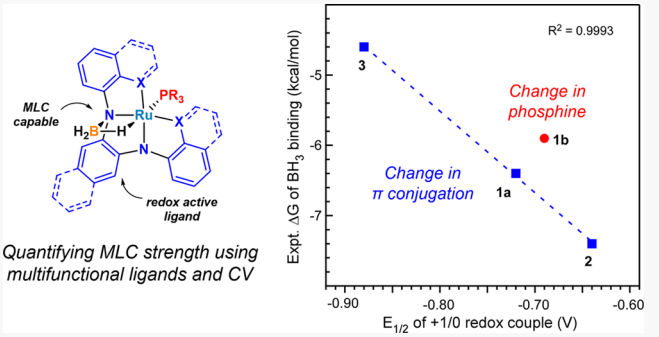


Downloaded via UNIV OF IOWA on June 11, 2022 at 15:18:36 (UTC).
See https://pubs.acs.org/sharingguidelines for options on how to legitimately share published articles.

## INTRODUCTION

Metal–ligand cooperativity (MLC) refers to a growing class of chemical reactions that rely on the synergistic participation of metals and reactive ligands to achieve a chemical transformation.[1] Traditional examples of MLC have centered around complexes containing nucleophilic ligand atoms that assist metals in substrate binding and bond cleavage, as reported for metal–ligand bifunctional catalysts and metalloenzymes.[2] However, MLC has expanded rapidly over the past decade to include ligand scaffolds that leverage (de)aromatization reactivity[1c,3] and Lewis acid functional groups.[4] Moreover, the concept of cooperativity with respect to MLC has continued to be refined,[5] and expansion of the term has been suggested to include synergistic reactions involving main group elements (element–ligand cooperativity)[6] and redox-active ligands that provide electron equivalents but do not directly participate in substrate binding and subsequent chemical steps.[1i,7]

As part of our growing interest in new facets of MLC, we have been investigating how metal–ligand cooperative binding across M–N bonds affects the redox activity of noninnocent tetradentate ligands with more than one redox-active center. For example, we recently reported how the $N_2S_2$ ligand **L1** (Scheme 1), derived from *o*-phenylenediamine with well-documented redox activity,[8] can undergo multiple MLC binding events with $BH_3$ when coordinated to Ru. As observed with **L1**, $BH_3$ and other boranes are known to undergo MLC in a variety of complexes containing ligands with Lewis base donor sites. These reactions can occur with or without B–H bond cleavage and have been implicated in hydroboration reactions and insertion into metal–element bonds.[1h,9]

Our previous studies showed how the metal–ligand cooperative binding of $BH_3$ causes the stepwise attenuation of ligand-centered redox activity as it binds to one and two N atoms in Ru complexes with **L1**, as monitored by cyclic voltammetry (CV).[10] More significantly, CV data collected on isolated samples of **1a-BH$_3$** revealed that MLC binding was

**Received:** September 26, 2021
**Published:** January 24, 2022

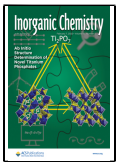


© 2022 American Chemical Society

https://doi.org/10.1021/acs.inorgchem.1c03014
*Inorg. Chem.* 2022, 61, 2391–2401

Scheme 1. (a) Electron-Transfer Series with L1 and (b) MLC Examples with Ru Complexes Containing L1 and $BH_3$[10]

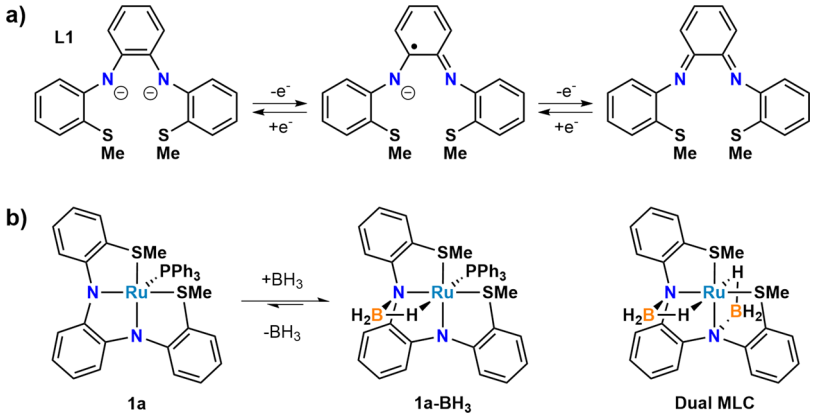


reversible under an applied potential to give equilibrium mixtures with and without $BH_3$. These results suggested that the multiple redox events associated with **L1** could be leveraged to quantify the MLC binding affinity using CV. Indeed, in situ electrochemical monitoring of the ligand-centered redox features as a function of differing $BH_3$ concentrations allowed the MLC binding affinity of $BH_3$ with **1a** to be quantified with $\Delta G = -6.4 \pm 0.4$ kcal/mol in THF.[10]

Building on our preliminary work with **1a**, we set out to determine if our electrochemical approach was sensitive enough to detect subtle MLC binding differences associated with changes in the redox-active ligand and supporting ancillary phosphine. In general, understanding how ligand modifications affect MLC binding strength is important when designing ligands that either enhance or suppress MLC depending on the desired application. Indeed, while desirable for many transformations, MLC has also been shown to eliminate productive catalytic pathways in certain situations, especially in reactions with $CO_2$.[11]

Here we report the synthesis and characterization of Ru complexes containing three different redox-active tetradentate ligands to examine how changes in ligand $\pi$ conjugation affect the MLC binding strength. **L2** extends the conjugation of the *o*-phenylenediamine backbone in **L1** by substituting it for 2,3-diaminonaphthalene, whereas **L3** extends the conjugation on the flanking groups while also changing the donor group from SMe to N (Chart 1). We also report the synthesis of the tricyclohexylphosphine ($PCy_3$) complex **1b**, which was prepared to evaluate how swapping out the $PPh_3$ ligand in **1a** trans to the open coordination site affects the MLC binding strength with **L1**. As we will show, this study demonstrates how CV can quantify subtle energetic differences in the MLC binding strength.

Chart 1. Numbering Scheme Used for Ligands Described in This Work

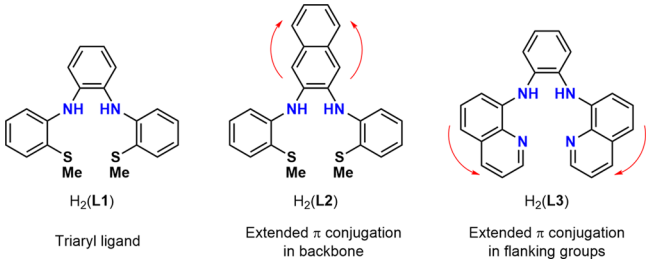


## RESULTS

**Synthesis and Characterization.** Ligands $H_2$(**L2**) and $H_2$(**L3**) were prepared using Buchwald-Hartwig cross-coupling reactions, similar to that described previously for $H_2$(**L1**).[12] The naphthalene derivative $H_2$(**L2**) was prepared by C−N coupling of 2,3-diaminonaphthalene with 2 equiv of 2-bromothioanisole using catalytic quantities of $Pd_2(dba)_3$ and BINAP in the presence of excess base. $H_2$(**L2**) was isolated in 67% yield after purification by column chromatography and subsequent recrystallization. The quinoline derivative $H_2$(**L3**) was prepared in a similar fashion by using *o*-phenylenediamine and 2 equiv of 8-bromoquinoline and was isolated in yields of up to 50%. The identity of both ligands was confirmed by microanalysis and NMR spectroscopy. The SMe groups in $H_2$(**L2**) are chemically equivalent on the NMR time scale and yield singlet resonances at $\delta$ 1.50 and 16.21 ppm for $^1$H and $^{13}$C, respectively. The N−H resonance for $H_2$(**L2**) was observed as a broadened singlet at $\delta$ 6.61 ppm in the $^1$H NMR spectrum, whereas the resonance for $H_2$(**L3**) was shifted to lower field at $\delta$ 8.22 ppm. The remaining peak positions and integrations for $H_2$(**L2**) and $H_2$(**L3**) were consistent with their conjugated aryl frameworks.

Next we prepared and characterized the 5-coordinate, 16-electron Ru(II) complexes targeted for MLC studies (Scheme 2). Ru(**L2**)$PPh_3$ (**2**) was prepared by treating a THF solution containing $H_2$(**L2**) and $RuCl_2(PPh_3)_3$ with 2 equiv of NaO$^t$Bu. This yielded a dark-blue/green solution from which dark-blue blocks of **2** could be isolated as single crystals in moderate yield (62%). Ru(**L3**)$PPh_3$ (**3**) was prepared similarly using a stepwise process. A THF solution of $H_2$(**L3**) with $RuCl_2(PPh_3)_3$ was first heated to reflux for 3 h to yield a green solution. After the solvent was removed and the green solid was washed thoroughly with pentane to remove liberated $PPh_3$, the solid was redissolved in THF and treated with 2 equiv of K[N(SiMe$_3$)$_2$] to yield a dark-blue solution. Single crystals of **3** were isolated by crystallization from toluene in 67% yield. Failure to remove the $PPh_3$ byproduct in the synthesis of **3** prior to deprotonation with base instead yields the six-coordinate Ru(**L3**)$(PPh_3)_2$ (**4**), which was confirmed by single-crystal XRD and subsequent NMR analysis (see below).

To prepare Ru(**L1**)$PCy_3$ (**1b**), we first attempted to simply exchange $PPh_3$ in **1a** for $PCy_3$ following procedures similar to



https://doi.org/10.1021/acs.inorgchem.1c03014
Inorg. Chem. 2022, 61, 2391−2401

**Scheme 2. Synthesis and Numbering Scheme Used for MLC-Free Ru Complexes**

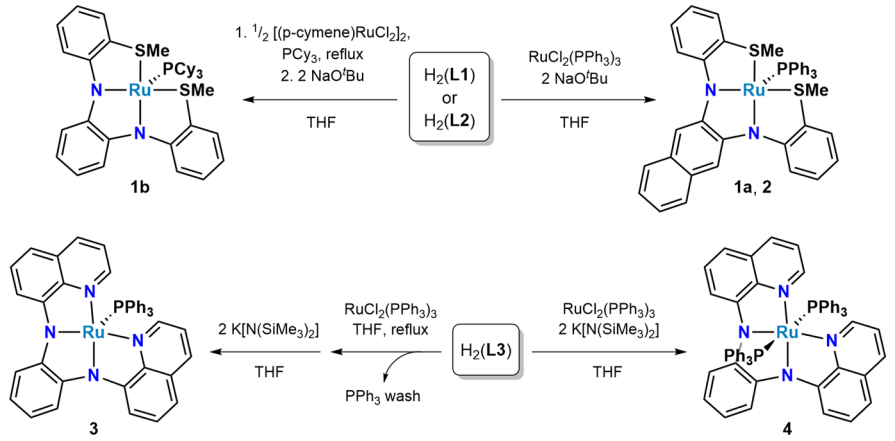


**Table 1. Selected Bond Distances (Å) from Single-Crystal XRD Data (E = N or S)**

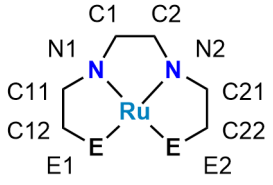


| | 1a[a] | 1a-$BH_3$[a] | 1b | 1b-$BH_3$ | 2 | 2-$BH_3$ | 3 | 3-$BH_3$ |
|---|---|---|---|---|---|---|---|---|
| Ru−N1 | 2.008(6) | 2.039(4) | 2.024(2) | 2.046(3) | 2.009(3) | 2.042(3) | 1.991(2) | 1.998(4) |
| Ru−N2 | 2.009(6) | 2.097(4) | 2.007(2) | 2.100(3) | 2.015(3) | 2.093(2) | 1.991(2) | 2.050(5) |
| Ru−E1 | 2.329(2) | 2.327(1) | 2.3160(7) | 2.317(1) | 2.331(1) | 2.3270(8) | 2.106(2) | 2.088(5) |
| Ru−E2 | 2.322(2) | 2.316(1) | 2.3225(9) | 2.304(1) | 2.315(1) | 2.3205(8) | 2.091(2) | 2.103(4) |
| Ru−P | 2.196(2) | 2.317(1) | 2.2375(6) | 2.375(1) | 2.202(1) | 2.3199(9) | 2.1998(6) | 2.310(1) |
| Ru−B | | 2.384(6) | | 2.371(4) | | 2.356(4) | | 2.350(5) |
| Ru−H | | 1.77(4) | | 1.73(4) | | 1.79(6) | | 1.97(3) |
| C1−C2 | 1.453(10) | 1.449(4) | 1.437(4) | 1.427(5) | 1.438(6) | 1.452(5) | 1.440(3) | 1.439(9) |
| N1−C1 | 1.39(1) | 1.385(5) | 1.401(3) | 1.393(5) | 1.419(5) | 1.388(4) | 1.405(3) | 1.390(8) |
| N2−C2 | 1.39(1) | 1.465(6) | 1.403(4) | 1.461(5) | 1.422(5) | 1.461(5) | 1.404(3) | 1.461(6) |
| N1−C11 | 1.39(1) | 1.374(6) | 1.391(3) | 1.359(5) | 1.374(5) | 1.368(4) | 1.382(3) | 1.370(9) |
| N2−C21 | 1.41(1) | 1.452(6) | 1.384(4) | 1.448(5) | 1.378(5) | 1.455(4) | 1.375(3) | 1.444(7) |
| N−B | | 1.611(7) | | 1.607(6) | | 1.590(4) | | 1.626(8) |

[a]From ref 10.

those reported by Grubbs and co-workers,[13] but these reactions were unsuccessful. Instead, a modified synthesis starting with phosphine-free $[(p\text{-cymene})RuCl_2]_2$ was required. $H_2$(**L1**) and $PCy_3$ were refluxed with 0.5 equiv of dimeric $[(p\text{-cymene})RuCl_2]_2$. Evaporating the mixture to dryness yielded a green solid that was subsequently treated with 2 equiv of $NaO^tBu$ in THF to yield **1b** in 68% yield after workup and crystallization.

Single-crystal XRD studies confirmed the synthesis of **1b**, **2**, and **3** and revealed the anticipated square-pyramidal coordination geometry for all three complexes (Figures S1−S3 in the SI). Selected bond distances are presented in Table 1. The Ru−N bond distances range from 1.991(2) to 2.024(2) Å and are consistent with the relatively short Ru−N bonds expected due to the $\pi$-donor properties of the amido groups. The Ru−S bonds in **1b** and **2** range from 2.315(1) to 2.331(1) Å and are typical of $Ru^{II}$−thioether distances.[14] Likewise, the Ru−$N_{quin}$ distances associated with the flanking quinoline groups in **3** are 2.088(5) and 2.103(4) Å, which compare well to those observed in Ru(II) complexes containing a quinoline-based pincer ligand.[15] The Ru−$PPh_3$ distances in **1a**, **2**, and **3** are identical within error at 2.20 Å, but the substitution of $PCy_3$ in **1b** increases the Ru−P distance by ca. 0.04 Å to 2.2375(6) Å.

Solution NMR spectra collected for **1b**, **2**, and **3** corroborated their solid-state structures. The $^1$H NMR data for all three complexes were relatively unremarkable aside from the sharp $^1$H resonances for **1b** in $C_6D_6$. This is notable because **1a** exhibited $^1$H NMR resonances that were too broad to be observed at RT due in part to the fluxionality of the SMe groups. The differences in RT resolution are attributed to the added sterics of $PCy_3$ vs $PPh_3$ that attenuates different stereoisomers possible based on the orientation of the SMe groups in solution. Similarly, the $^{31}$P NMR spectrum of **1b** revealed a sharp singlet at $\delta$ 88.1 ppm that is only slightly upfield of the broad peak observed for **1a** at $\delta$ 89.9 ppm despite the difference in phosphine. Like **1a**, the analysis of **3** in noncoordinating solvents (e.g., benzene) results in a lower field and broadened $^{31}$P peak at $\delta$ 86.8 ppm (fwhm = 650 Hz). This broad $^{31}$P peak for **3** shifts to $\delta$ 75.0 ppm and sharpens slightly in THF-$D_8$ (fwhm = 300 Hz), suggesting that THF is likely occupying the open coordination site trans to $PPh_3$. This is


https://doi.org/10.1021/acs.inorgchem.1c03014
Inorg. Chem. 2022, 61, 2391−2401

**Scheme 3. Synthesis of MLC-Bound $BH_3$ Complexes**

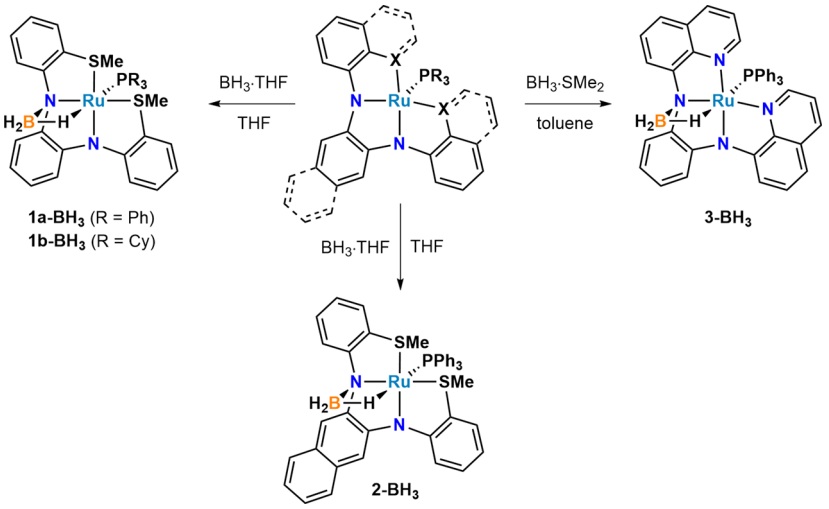


notable because we do not see evidence of THF binding to the open coordination sites in **1a**, **1b**, and **2**, presumably due in part to the steric protection afforded by the picketed SMe groups projecting away from $PPh_3$ and $PCy_3$.

Even though THF appears to bind to **3** when dissolved in THF, attempts to isolate this complex were unsuccessful. Crystallization from solutions containing THF yielded only crystals of THF-free **3**. However, as mentioned above, the stronger field ligand $PPh_3$, which is liberated from the $Ru(PPh_3)_3Cl_2$ starting material used to prepare **3**, will bind to the open coordination site in **3** to form **4** if not removed prior to the deprotonation of $H_2$(**L3**). The identity of **4** was confirmed by single-crystal XRD data collected on crystals grown from pentane/THF to reveal an octahedral complex with two $PPh_3$ ligands occupying the axial sites (Figure S4 in the SI). The Ru−P distances for **4** are significantly longer at 2.395(1) and 2.388(1) Å compared to that for **3** (2.1998(6) Å). The Ru−N distances also lengthen slightly, by about ∼0.02 Å, and only subtle changes are observed in the ligand.

The $^1$H NMR integrations of **4** in THF-$D_8$ confirmed the presence of two $PPh_3$ ligands, but no resonances were observed in the $^{31}$P NMR spectrum, which suggests that $PPh_3$ exchange may be occurring at the metal in coordinating THF. Indeed, switching to noncoordinating solvents such as toluene and benzene revealed a broad resonance at $\delta$ 27.5 ppm (fwhm = 300 Hz), which is a significantly higher field compared to that of **3** at $\delta$ 86.8 ppm in benzene.

**Synthesis and Characterization of MLC Complexes.** MLC complexes with $BH_3$ were synthesized by the addition of $BH_3$·THF in THF (**1b-BH$_3$** or **2-BH$_3$**) or $BH_3$·$SMe_2$ in toluene (**3-BH$_3$**) to the corresponding parent complex (Scheme 3). The reactions occur rapidly: the addition of $BH_3$·THF to **1b** and **2** caused an immediate color change from dark blue to yellow. Likewise, the addition of $BH_3$·$SMe_2$ to **3** caused the solution to change from dark red to dark blue. All three complexes were isolated as single crystals suitable for XRD after workup and crystallization.

Single-crystal XRD studies confirmed $BH_3$ binding across one of the Ru−N bonds and permitted a structural comparison for each MLC complex (Figure 1). As observed with **1a-BH$_3$**, the engagement of the N lone pair in MLC binding eliminates N → Ru $\pi$-donation and causes the Ru−N bond to elongate in all of the complexes: the Ru−N distances increased from

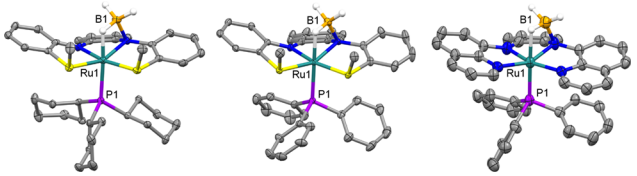


**Figure 1.** Molecular structures of **1b-BH$_3$** (left), **2-BH$_3$** (center), and **3-BH$_3$** (right). Thermal ellipsoids are drawn at the 50% level. Hydrogens attached to carbon were omitted.

2.007(2) to 2.100(3) Å (**1b-BH$_3$**), 2.015(3) to 2.093(2) Å (**2-BH$_3$**), and 1.991(2) to 2.050(5) Å (**3-BH$_3$**). The Ru−P distances also lengthened by ∼0.1 Å due to B−H occupation in the open coordination site trans to the P atom.

MLC binding also causes significant changes in the ligand bond distances. As expected, the most pronounced change is observed for the N2−C2 and N2−C21 bond distances, which lengthen by 0.05 to 0.07 Å as N2 engages in MLC. The newly formed N−B bonds vary and decrease in the order of 1.626(8) Å (**3-BH$_3$**), 1.611(7) Å (**1a-BH$_3$**), 1.607(6) Å (**1b-BH$_3$**), and 1.590(4) Å (**2-BH$_3$**), suggesting that the N → B donor−acceptor strength increases in the order of **3** < **1a** ≈ **1b** < **2**.

NMR spectroscopy was used to further investigate the presence of MLC binding for each of the complexes in solution, and the most relevant data are compiled in Table 2. The $^{31}$P NMR resonance for **1b** at $\delta$ 88.1 ppm shifts to higher field at $\delta$ 38.4 ppm and splits into a doublet for **1b-BH$_3$** due to trans P−Ru−H coupling ($^2J_{PH}$ = 60 Hz). A corresponding broad doublet assigned as the Ru−H−B bridging hydride appeared in the $^1$H NMR spectrum at $\delta$ −7.38 ppm ($^2J_{PH}$ = 60 Hz). Terminal B−H signals were too broad to be observed in

**Table 2. Selected NMR and IR Spectroscopic Data for 1a-BH$_3$, 1b-BH$_3$, 2-BH$_3$, and 3-BH$_3$[a]**

| | $^1$H (Ru−H) | $^{31}$P | $^{11}$B | B−H stretches (cm$^{-1}$) |
|---|---|---|---|---|
| **1a-BH$_3$** | −6.28 (60) | 51.1 | −12.2 | 2430, 2404, 2338 |
| **1b-BH$_3$** | −7.38 (60) | 38.4 | −11.5 | 2431, 2406, 2338 |
| **2-BH$_3$** | −6.45 (67) | 49.8 | −12.6 | 2460, 2414, 2338 |
| **3-BH$_3$** | −4.57 (br) | 47.5 | −13.7 | 2416, 2393, 2318 |

[a]NMR data are reported in $C_6D_6$ except for 3-BH$_3$ (DCM and THF). $^2J_{HP}$ values are shown in Hz in parentheses.



https://doi.org/10.1021/acs.inorgchem.1c03014
Inorg. Chem. 2022, 61, 2391−2401

the $^{1}$H NMR spectrum, but the $^{11}$B NMR spectrum revealed a broad signal at $\delta$ −11.5 ppm (fwhm = 150 Hz). The $^{31}$P NMR spectrum of **2-BH$_3$** similarly resulted in a doublet at $\delta$ 49.8 and a low-intensity broad resonance in the $^{11}$B NMR at $\delta$ −12.6 ppm (fwhm = 250 Hz). The analysis of the $^{1}$H NMR spectrum for **2-BH$_3$** revealed a doublet at $\delta$ −6.45 ppm ($^{2}J_{PH}$ = 67 Hz) due to the trans P−Ru−H coupling and broad resonances in the baseline at $\delta$ 1.89 and 2.79 ppm that account for terminal B−H. The $^{31}$P NMR spectrum of **3-BH$_3$** in DCM resulted in a broad resonance at higher field at $\delta$ 47.5 ppm (fwhm = 80 Hz), and the $^{11}$B NMR spectrum revealed a broad resonance at $\delta$ −13.7 ppm (fwhm = 350 Hz).

The MLC complexes were characterized by IR spectroscopy to further evaluate the strength of MLC with BH$_3$. Each complex displays three BH$_3$ stretching absorptions in the B−H stretching region (~2200−2500 cm$^{-1}$). The low-energy absorption in each spectrum is assigned to the B−H−Ru stretch, whereas those at higher wavenumbers are assigned to the symmetric and asymmetric terminal B−H stretches (Figure 2). The three B−H stretches for **1a** and **1b** are almost

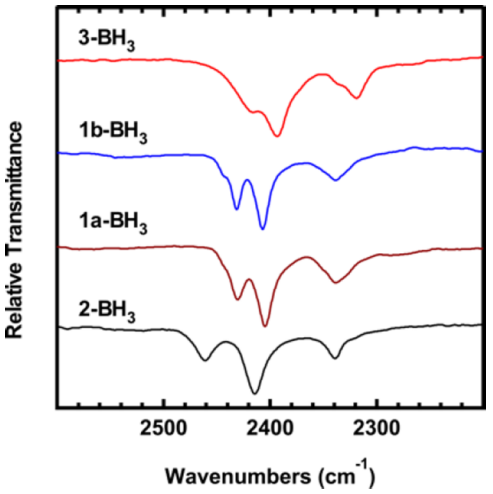


**Figure 2.** IR spectra (B−H stretching region) of the MLC complexes.

identical, indicating that changing the identity of the phosphine has no significant effect on the energy of BH$_3$ stretching modes. In contrast, **2-BH$_3$** displays blue-shifted terminal B−H stretches at 2460 and 2414 cm$^{-1}$ compared to those for **1a-BH$_3$** and **1b-BH$_3$**, whereas those for **3-BH$_3$** are red-shifted and broader at 2416 and 2393 cm$^{-1}$. Moreover, the B−H−Ru stretch for **2-BH$_3$** is identical to those for **1a-BH$_3$** and **1b-BH$_3$** at 2338 cm$^{-1}$, whereas the bridging B−H bond in **3-BH$_3$** appears at slightly lower energy (2318 cm$^{-1}$).

**Electrochemical Studies.** Cyclic voltammetry (CV) studies and BH$_3$·THF titrations were performed to quantify how ligand modification affects the redox activity and MLC binding properties of **1b**, **2**, and **3** for comparison to those of **1a**. CV data collected on each complex revealed two quasi-reversible waves with $E_{1/2}$ values ranging from −0.88 to −0.16 V vs Fc/Fc$^{+}$ assigned primarily to ligand-centered redox activity localized on the *o*-phenylenediamine or 2,3-diaminonaphthalene backbones (Figure 3 and Table 3). The most negative wave in this window is attributed to the +1/0 redox couple, which follows the order **3** < **1a** < **1b** < **2**, whereas the wave at more positive potentials is attributed to the +2/+1 redox couple.[16]

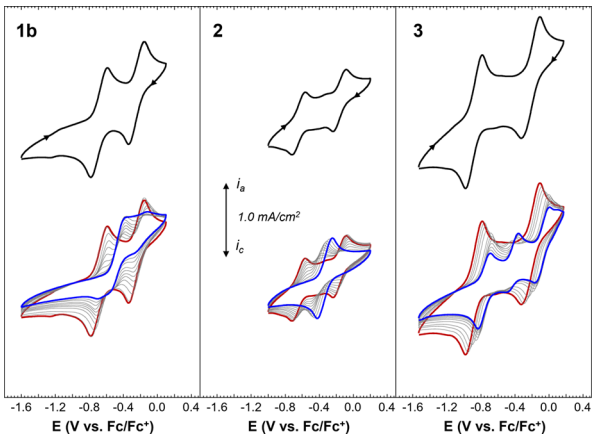


**Figure 3.** (Top) Truncated CVs of **1b**, **2**, and **3** collected at 100 mV/s. (Full scans of the solvent window can be found in the SI.) (Bottom) CV titration studies showing the addition of 0.1 mol equiv of BH$_3$·THF to solutions of **1b**, **2**, and **3**. The initial scans are shown in red, and the final scans with 1.0 mol equiv of BH$_3$·THF are shown in blue. All CV data were collected in THF with a 0.1 M ($^{n}$Bu$_4$N)PF$_6$ supporting electrolyte using a glassy carbon working electrode and a Pt wire as the counter and quasi-reference electrodes, respectively.

**Table 3. CV Data Collected in THF at 100 mV/s**[a]

| | $E_{1/2}$ (V) | $E_{pa} - E_{pc}$ (V) | $I_{pc}/I_{pa}$ |
|---|---|---|---|
| **1a** | −0.72 | 0.16 | 0.98 |
| | −0.25 | 0.16 | 0.95 |
| **1b** | −0.69 | 0.20 | 1.08 |
| | −0.25 | 0.19 | 1.00 |
| **2** | −0.64 | 0.16 | 1.07 |
| | −0.16 | 0.16 | 1.11 |
| **3** | −0.88 | 0.20 | 1.19 |
| | −0.21 | 0.22 | 0.92 |
| **1a-BH$_3$** | −0.50 | 0.13 | 0.62 |
| **1b-BH$_3$** | −0.45 | 0.31 | 0.44 |
| **2-BH$_3$** | −0.33 | 0.18 | 0.93 |
| **3-BH$_3$** | −0.42 | 0.16 | 0.49 |

[a]Potentials are referenced to Fc/Fc$^{+}$.

Although not monitored in the titration studies described below, additional features assigned to the 0/−1 redox couple were observed at more negative potentials for **1a**, **1b**, **2**, and **3** and range from −2.90 to −2.30 V vs Fc/Fc$^{+}$ (SI). These features were irreversible for **1a**, **1b**, and **2** and reversible for **3** with quinoline-derived **L3**. Irreversible redox features at similarly negative potentials have been assigned to Ru(II/I) redox couples in complexes with thioether-based SNS pincer ligands,[14c] and an analysis of the Kohn−Sham orbitals obtained from our DFT calculations (details described below) suggests a similar assignment. The calculated LUMO of **1a**, **1b**, and **2** is primarily Ru−P $\sigma$* from PPh$_3$ mixing with the Ru 4d$_{z^2}$ (Figure 4). The LUMO for **3** also contains the Ru 4d$_{z^2}$, but it shows more mixing with the $\pi$ orbitals on the flanking quinoline groups and no appreciable Ru−P $\sigma$* character. The population of the Ru−P $\sigma$* in **1a**, **1b**, and **2** during reduction, perhaps with corresponding PPh$_3$ loss, could account for the irreversibility of their 0/−1 redox couples when compared to **3** with no Ru−P $\sigma$* in the LUMO. Similar arguments were made to rationalize the irreversible CV reductions observed with the aforementioned Ru(II) SNS pincer complexes.[14c]


https://doi.org/10.1021/acs.inorgchem.1c03014
Inorg. Chem. 2022, 61, 2391−2401

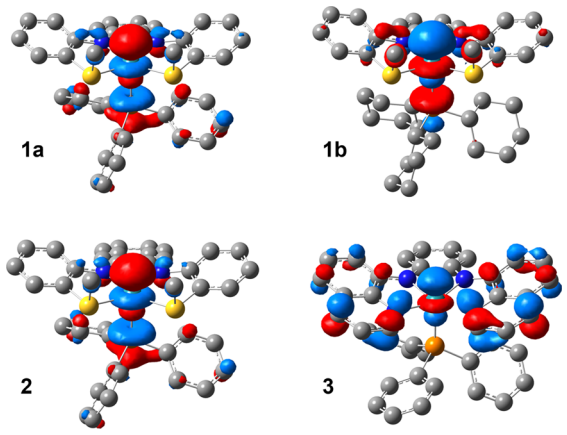


**Figure 4.** Kohn–Sham orbital plots of the LUMO for **1a**, **1b**, **2**, and **3** plotted for the same isovalues.

MLC engagement with $BH_3$ in **1b**, **2**, and **3** eliminates one of the two redox features observed for the parent complexes and shifts the potential so that it lies between the two parent peaks. This is clear in the CV collected on isolated crystals of **2-BH$_3$** (Figure S10, SI), which shows a single reversible feature at −0.30 V compared to the two features in the CV of **2** at −0.64 and −0.16 V (Table 3). As discussed in more detail below, the change from two redox features to one is due to the engagement of a N atom on the ligand, which takes the flanking aryl group out of the $\pi$ conjugation with the rest of the ligand framework.

We next monitored the electrochemical changes as a function of added $BH_3$·THF (which is electrochemically inert in the CV window shown). As with **1a**, the kinetics of $BH_3$ binding with **1b**, **2**, and **3** are fast and are assumed to be at equilibrium during the CV measurements. (This was tested by taking multiple CVs for each point that exhibits a stable/reproducible response.) This allowed $\Delta G$ values to be determined for the MLC binding affinity associated with each complex. The CV titration data showed significant differences in the MLC-binding equilibrium under an applied potential. **2** completely converts to **2-BH$_3$**, as indicated by the clean conversion from two redox features to one, whereas **1b** and **3** did not fully convert even in the presence of excess $BH_3$·THF (Figure 3). Modeling the CV titration data (Supporting Information) yielded $\Delta G$ values of −7.4 ± 0.4 (**2**), −5.9 ± 0.4 (**1b**), and −4.6 ± 0.3 kcal/mol (**3**). When combined with the value previously determined for **1a** (−6.4 ± 0.4 kcal/mol), this gives an experimental ranking of MLC strength of **2** > **1a** ≈ **1b** > **3**.

**DFT Calculations.** Dispersion-corrected DFT calculations (B3LYP-d3) were used to calculate the solution-phase Gibbs free energies of MLC binding using $BH_3$·THF for comparison to the experimental $\Delta G$ values. One of the advantages of DFT is that the Gibbs free energy can be calculated for both the neutral and oxidized complexes in discrete steps (eqs 1 and 2). By comparison, the experimental CV titration data cannot discriminate between these individual steps and accounts only for the total concentration of the complex with or without MLC.

$$[M] + BH_3{\cdot}THF \rightarrow [M{-}BH_3] + THF \quad (1)$$

$$[M]^{1+} + BH_3{\cdot}THF \rightarrow [M{-}BH_3]^{1+} + THF \quad (2)$$

All molecules were optimized in the gas phase with solvent corrections derived from a polarizable continuum model for THF to ultimately give the values used in the standard-state Gibbs free energy calculations. Calculated bond distances in the optimized gas-phase structures are slightly overestimated when compared to the experimental solid-state XRD data, as is typical of hybrid GGA functionals such as B3LYP.[17] In general, the bond distances follow the same experimental trends (Tables S3 and S4, SI), but the differences associated with MLC-bound $BH_3$ are not as pronounced when compared to the XRD values. N–B distances in the calculated neutral $BH_3$ complexes are nearly identical within error and range from 1.597 to 1.603 Å ($\Delta$ = 0.006 Å) compared to the experimental values of 1.590(4)–1.626(8) Å ($\Delta$ = 0.036 Å). Likewise, the calculated Ru–H distances in these complexes are practically identical, ranging from 1.767 to 1.772 Å. A similar lack of variation is observed for N–B and Ru–H bond distances in the calculated structures of the singly oxidized $BH_3$ complexes.

Although DFT results reveal only subtle variations in N–B and Ru–H bond distances that would otherwise suggest smaller differences in the MLC binding strength, the calculated $\Delta G$ values provided in Table 4 show more significant differences that are in good agreement with the experimental trends. The transfer of $BH_3$ from $BH_3$·THF to all of the neutral complexes (eq 1) is exergonic and relatively close to the experimentally determined values. The most negative $\Delta G$ for the neutral complexes was calculated for **1a** at −7.1 kcal/mol, and the values followed the order **1a** < **2** < **1b** < **3**. Interestingly, the binding becomes less favorable by ca. 3 to 4 kcal/mol when **1a**, **1b**, and **3** are oxidized but is identical for **2** and **2**$^+$ at −5.9 kcal/mol. (The reason for these differences will be discussed below.) This gives the ordering **2**$^+$ < **1a**$^+$ < **1b**$^+$ < **3**$^+$, in alignment with the experimentally observed trend in $\Delta G$.

**Table 4. Comparison of Experimental $\Delta G$ from CV Titration Studies with $BH_3$·THF and Calculated $\Delta G$ of Reaction Values Corresponding to Equations 1 and 2**[a]

| | 2 | 1a | 1b | 3 |
|---|---|---|---|---|
| expt | −7.4 ± 0.4 | −6.4 ± 0.4 | −5.9 ± 0.4 | −4.6 ± 0.3 |
| eq 1 | −5.9 | −7.1 | −4.1 | −4.2 |
| eq 2 | −5.9 | −3.3 | −1.3 | 0.0 |

[a]All values are reported in kcal/mol.

Another possibility we had to consider in evaluating the thermodynamics of MLC binding was the possibility of THF (the solvent used to collect the electrochemistry data) competing with $BH_3$ for the open coordination site in the Ru complexes. We did not see any experimental evidence of THF binding to the open coordination site trans to $PPh_3$ in **1a** in previous studies,[10,12] and the same goes here for **1b** and **2**. The complexes can be crystallized from THF, and their spectroscopic data shows no remarkable differences when collected in THF compared to collection in other solvents such as $C_6D_6$. These observations are consistent with the $\Delta G$ values calculated for THF binding, which are close to thermoneutral for **1a**, **1b**, and **2** (Table S5, SI). In contrast, the reduced sterics of **L3** and the ability of **3** to bind an extra equivalent of $PPh_3$ to form **4** suggested that THF binding was more likely to occur with **3**. Indeed, as mentioned above, **3** undergoes a color change from dark red to dark blue when dissolved in THF, and NMR data collected on these solutions revealed a significant shift in the $^{31}$P resonance from $\delta$ 86.8 to 75.0 ppm. Consistent


https://doi.org/10.1021/acs.inorgchem.1c03014
Inorg. Chem. 2022, 61, 2391–2401

with this observation, THF binding to **3** was calculated to be exergonic at −6.5 kcal/mol (Table S5, SI).

When starting with THF bound to the metals in the neutral and oxidized complexes, the calculated $\Delta G_{MLC}$ values follow the same trend observed experimentally. However, there is a larger deviation between the experimental and calculated values starting with bound THF, especially for **3** and $\mathbf{3}^+$. These larger differences suggest that competitive THF binding is not a significant factor under the experimental CV conditions. (See the SI for the data and a more detailed discussion.)

Returning to the question as to why the calculated $\Delta G$ values of $BH_3$ binding for neutral and oxidized **2** are identical and those for **1a**, **1b**, and **3** are not, we can look to the frontier Kohn−Sham orbitals for a possible explanation. The approximate point group symmetry for all four complexes is $C_s$ if one ignores the substituents attached to phosphorus. Consistently, the $\pi$-electron density in the frontier orbitals of **1a**, **1b**, and **3** is relatively symmetric with respect to the $C_s$ mirror plane (Figure 5). However, an analysis of the HOMO

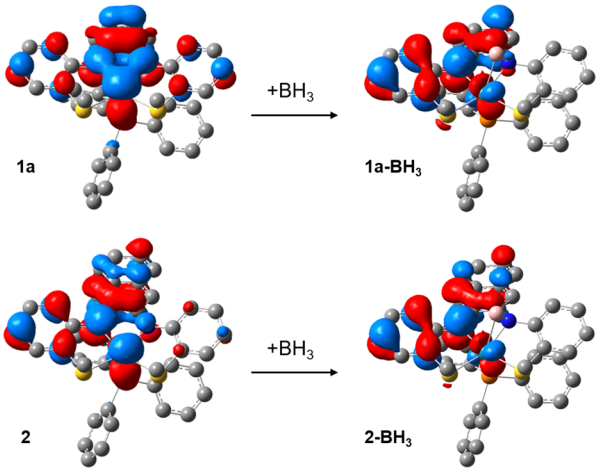


**Figure 5.** Kohn−Sham orbital plots of the HOMO for (top) **1a** and **1-BH$_3$** and (bottom) **2** and **2-BH$_3$**. Hydrogen atoms were omitted for easier viewing of the orbital density.

of **2** reveals that the $\pi$-electron density is not delocalized symmetrically over both N atoms and flanking aryl groups and instead preferentially localizes on half of the ligand. This asymmetry seems to arise from the extended naphthyl backbone in **2** combined with the 3-fold phenyl substituents on $PPh_3$. Calculations where $PPh_3$ in **2** was replaced with smaller $PMe_3$, for example, restored the $C_s$ symmetry in the frontier orbitals (Figure S21, SI). Further corroboration of the $\pi$-orbital asymmetry for **2** is observed in the Mulliken spin density values in the singly oxidized complexes. Calculated spin densities on the N atoms for $\mathbf{2}^+$ are 21.1 and 13.8% (a difference of 7.3%), whereas those for $\mathbf{1a}^+$, $\mathbf{1b}^+$, and $\mathbf{3}^+$ are more symmetric, exhibiting smaller differences that range from 1.4 to 2.1% (Table 5).

The most serious consequence of the asymmetry observed in the ligand $\pi$ distribution in the HOMO of **2** is that there is less of a change to the $\pi$ conjugation in **L2** upon $BH_3$ binding compared to **1a**, **1b**, and **3**. As exemplified by **1a** in Figure 5, MLC binding takes the N lone pair and the associated flanking aryl group out of the $\pi$ conjugation with the rest of the ligand framework. In contrast, $BH_3$ binding to **2** has less of an effect on the ligand $\pi$ redistribution because the asymmetry is already

**Table 5. Calculated Mulliken Spin Densities for Ru and N[a]**

| | Ru | N1 | N2 | total N |
|---|---|---|---|---|
| $\mathbf{1a}^+$ | 27.4% | 19.0% | 17.5% | 36.5% |
| $\mathbf{1b}^+$ | 36.8% | 17.7% | 15.9% | 33.6% |
| $\mathbf{2}^+$ | 31.1% | 21.1% | 13.8% | 34.9% |
| $\mathbf{3}^+$ | 42.1% | 16.5% | 14.4% | 30.8% |
| **1a-BH$_3$**$^+$ | 22.6% | 41.5% | 0.1% | 41.6% |
| **1b-BH$_3$**$^+$ | 27.9% | 39.9% | −0.1% | 39.8% |
| **2-BH$_3$**$^+$ | 20.9% | 40.9% | −0.3% | 40.6% |
| **3-BH$_3$**$^+$ | 34.0% | 32.7% | −0.5% | 32.2% |

[a]Spin density plots and a full list of values for all atoms are provided in the Supporting Information.

present in the $\pi$ manifold to start. The implications of this asymmetry appear to be even more significant when the complexes are oxidized to generate ligand-centered radicals. We posit that oxidizing **1a-BH$_3$**, **1b-BH$_3$**, and **3-BH$_3$** provides an additional driving force for $BH_3$ loss because doing so allows the radical to be delocalized over both N atoms as well as the remaining ligand framework (Scheme 4). In contrast,

**Scheme 4. $\pi$ Delocalization (in Red) in the HOMO of $\mathbf{1a}^+$ (Top) and $\mathbf{2}^+$ (Bottom) with and without MLC[a]**

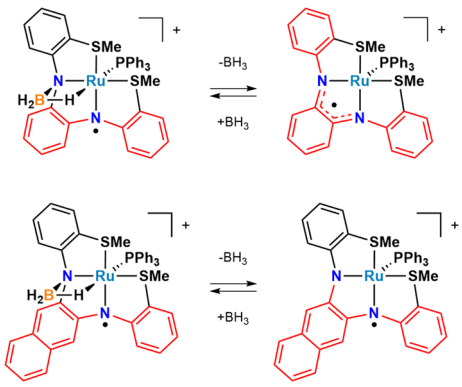


[a]The depiction is based on calculated spin density plots shown in Figures S17−S20 in the SI, and it mirrors the calculated HOMO orbital plots shown in Figure 5.

resonance delocalization is not improved significantly when $BH_3$ is lost from **2-BH$_3$**$^+$ because of the asymmetry inherently present in the $\pi$ manifold of $\mathbf{2}^+$. This appears to be why the DFT calculations suggest that $\Delta G$ does not change for neutral and oxidized **2** but does so for **1a**, **1b**, and **3**.

## DISCUSSION

The DFT studies suggest that differences in the extent of N $\pi$ delocalization, especially before and after oxidation, account for the key differences in MLC binding strength, as measured by CV. Given that the N atoms on the ligand are heavily involved in both MLC and ligand-centered redox activity and because the ligand-centered redox activity should also be affected by differences in ligand $\pi$ delocalization, we suspected that the electrochemical potentials should correlate to the MLC binding strength. To test this hypothesis, we plotted the experimental $\Delta G$ values vs the +1/0 redox potentials. Gratifyingly, the plot reveals a remarkable linear trend ($R^2$ = 0.9993) between the $PPh_3$-containing complexes containing **1a**, **2**, and **3** despite the changes in the identity of redox-active ligands (Figure 6a).


https://doi.org/10.1021/acs.inorgchem.1c03014
Inorg. Chem. 2022, 61, 2391−2401

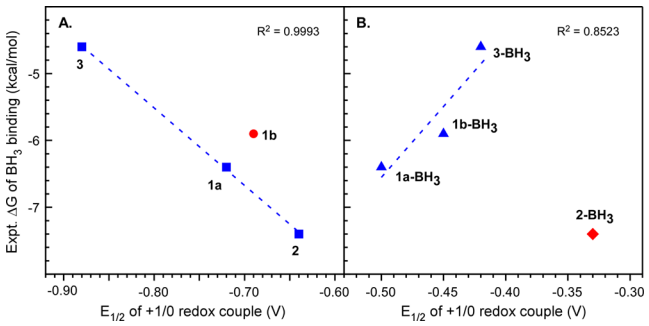


**Figure 6.** Comparison of experimental $\Delta G$ of $BH_3$ binding from CV titration studies vs $E_{1/2}$ of the 0/+1 redox couple for the (A) $BH_3$-free complexes and (B) $BH_3$ complexes. The points in blue were included in the linear regression for each plot.

The plot in Figure 6a shows how the $\Delta G$ of $BH_3$ binding increases as the $E_{1/2}$ is pushed to more positive potentials. **3** is the easiest to oxidize (most negative +1/0 potential at −0.88 V), which suggests that the ligand better stabilizes the generated radical relative to the other complexes due to increased $\pi$ delocalization. Consistent with this interpretation, increased $\pi$ delocalization should diffuse electron density associated with the N lone pair to make it less nucleophilic, which aligns with **3** having the weakest MLC binding strength. On the opposite end, **2** is the hardest to oxidize in the series (−0.64 V) because of its decreased $\pi$ delocalization. This aligns with the N atoms being the most nucleophilic, as indicated by the strongest $BH_3$ binding strength.

Because MLC involves coordination at sites on the metal and the ligand, it can be difficult to tease out their individual contributions to the MLC binding strength. The plot in Figure 6a suggests that these contributions may be distinguished on the basis of the identity of the ancillary phosphine. Swapping $PPh_3$ in **1a** for $PCy_3$ in **1b** appears to weaken the MLC binding relative to its projected position based on its oxidation potential and the linear regression defined by **1a**, **2**, and **3** in Figure 6a. This weakening could be consistent with the more strongly $\sigma$-donating $PCy_3$ acting on the Ru−H bond. Another possibility, however, is that the different donor−acceptor properties of the $PCy_3$ ligand are altering the redox potential of **1b** compared to that of **1a** more so than the MLC strength. We cannot rule out either possibility on the basis of the data provided.

We next performed the same analysis using the $E_{1/2}$ values for the +1/0 couple in the $BH_3$ complexes. The $\Delta G$ vs $E_{1/2}$ plot in Figure 6b shows a good linear correlation for the complexes containing diaminobenzene-derived **L1** and **L3** ($R^2$ = 0.8523), whereas **2-BH$_3$** with diaminonaphthalene-derived **L2** falls off the line with a significantly more exergonic $\Delta G$. This corroborates the DFT findings showing that the $\Delta G$ values of binding for both neutral and oxidized **2** are uniquely similar, whereas the binding becomes less favorable by 3 to 4 kcal/mol when **1a**, **1b**, and **3** are singly oxidized. The linear correlation for these latter three complexes in Figure 6b shows that more positive potentials correlate to weaker $BH_3$ binding, which suggests that $BH_3$ is lost more readily as the complex becomes more difficult to oxidize. This is consistent with the energy offset hypothesis proposed for additional radical delocalization available for diaminobenzene ligands **L1** and **L3** without $BH_3$, as shown in Scheme 4. As the MLC complex becomes more difficult to oxidize, one would expect a greater driving force for $BH_3$ loss to stabilize the radical, which is achieved by allowing it to delocalize over more of the conjugated framework. In contrast, **2-BH$_3$** falls off the line because there is not a significant gain in radical delocalization when $BH_3$ is lost because of the inherent asymmetry always present in the $\pi$ manifold of **L2**.

## CONCLUSIONS

We have demonstrated a method for quantifying how relatively subtle ligand modifications affect metal−ligand cooperative (MLC) binding strength. A series of Ru complexes containing different redox-active tetradentate ligands were prepared and characterized by structural, spectroscopic, and electrochemical methods. CV titration studies with $BH_3$·THF allowed $\Delta G_{MLC}$ values with $BH_3$ to be quantified for each of the complexes. DFT calculations reproduced the experimental trend in the MLC binding strength, and the results suggest that changes in the symmetry and degree of $\pi$ conjugation in the redox-active ligands govern the MLC binding strength. This was corroborated by remarkably linear correlations between experimentally measured $\Delta G$ values and ligand-centered redox potentials.

A key component of the approach described here is the use of multifunctional ligands (i.e., those capable of both MLC and redox activity) as electrochemical reporters of the MLC binding strength. Given that there are many redox-active ligands known with MLC-capable functional groups and because CV is not an element- or isotope-specific technique, it is possible that our CV titration method could be used to quantify MLC substrate binding with a wider range of ligands, metals, and substrates. Given the sensitivity of CV, this approach may also be useful for identifying fleeting MLC complexes that are difficult to detect by other means, especially with more weakly binding MLC substrates such as $CO_2$.

## ASSOCIATED CONTENT

### Supporting Information

The Supporting Information is available free of charge at https://pubs.acs.org/doi/10.1021/acs.inorgchem.1c03014.

Experimental procedures, spectroscopic data, full CV scans, scan rate dependence plots, crystallographic data (PDF)

DFT-optimized structures (XYZ)

### Accession Codes

CCDC 2101494−2101500 contain the supplementary crystallographic data for this paper. These data can be obtained free of charge via www.ccdc.cam.ac.uk/data_request/cif, or by emailing data_request@ccdc.cam.ac.uk, or by contacting The Cambridge Crystallographic Data Centre, 12 Union Road, Cambridge CB2 1EZ, UK; fax: +44 1223 336033.

## AUTHOR INFORMATION

### Corresponding Authors

**Scott R. Daly** − *Department of Chemistry, The University of Iowa, Iowa City, Iowa 52242, United States;* orcid.org/0000-0001-6229-0822; Email: scott-daly@uiowa.edu

**Scott K. Shaw** − *Department of Chemistry, The University of Iowa, Iowa City, Iowa 52242, United States;* orcid.org/0000-0003-3767-3236; Email: scott-k-shaw@uiowa.edu

**Jason M. Keith** − *Department of Chemistry, Colgate University, Hamilton, New York 13346, United States;* orcid.org/0000-0002-5292-397X; Email: jkeith@colgate.edu



https://doi.org/10.1021/acs.inorgchem.1c03014
Inorg. Chem. 2022, 61, 2391−2401

### Authors

**Kyle D. Spielvogel** − *Department of Chemistry, The University of Iowa, Iowa City, Iowa 52242, United States*

**Nathan C. Stumme** − *Department of Chemistry, The University of Iowa, Iowa City, Iowa 52242, United States*

**Taylor V. Fetrow** − *Department of Chemistry, The University of Iowa, Iowa City, Iowa 52242, United States*

**Li Wang** − *Department of Chemistry, The University of Iowa, Iowa City, Iowa 52242, United States*

**Javier A. Luna** − *Department of Chemistry, The University of Iowa, Iowa City, Iowa 52242, United States*

Complete contact information is available at: https://pubs.acs.org/10.1021/acs.inorgchem.1c03014


### Author Contributions

S.R.D. and S.K.S. conceptualized and supervised the work. K.D.S. and N.C.S. completed the bulk of the experimental studies and curated the associated data. T.V.F. and L.W. prepared and characterized $H_2$(**L2**), and J.A.L. assisted with the electrochemical experiments. J.M.K. completed all the DFT calculations. S.R.D., K.D.S., and N.C.S. assembled the manuscript and Supporting Information, and all authors assisted with editing. All authors have given approval to the final version of the manuscript.

### Author Contributions

[§]K.D.S. and N.C.S. contributed equally.


### Funding

This work was generously supported by the National Science Foundation (CHE-1650894 and CHE-1651381).


### Notes

The authors declare no competing financial interest.

## ■ ACKNOWLEDGMENTS


We thank Dale Swenson for collecting the single-crystal XRD data. The National Science Foundation is also gratefully acknowledged for supporting the purchase of a new X-ray diffractometer under award CHE-1828117.


## ■ REFERENCES


(1) (a) Khusnutdinova, J. R.; Milstein, D. Metal-Ligand Cooperation. *Angew. Chem., Int. Ed.* **2015**, *54*, 12236−12273. (b) Li, H.; Zheng, B.; Huang, K.-W. A new class of PN3-pincer ligands for metal-ligand cooperative catalysis. *Coord. Chem. Rev.* **2015**, *293*−*294*, 116−138. (c) Zell, T.; Milstein, D. Hydrogenation and Dehydrogenation Iron Pincer Catalysts Capable of Metal-Ligand Cooperation by Aromatization/Dearomatization. *Acc. Chem. Res.* **2015**, *48*, 1979−1994. (d) Verhoeven, D. G. A.; Moret, M.-E. Metal-ligand cooperation at tethered π-ligands. *Dalton Trans.* **2016**, *45*, 15762−15778. (e) Omann, L.; Koenigs, C. D. F.; Klare, H. F. T.; Oestreich, M. Cooperative Catalysis at Metal-Sulfur Bonds. *Acc. Chem. Res.* **2017**, *50*, 1258−1269. (f) Alig, L.; Fritz, M.; Schneider, S. First-Row Transition Metal (De)Hydrogenation Catalysis Based On Functional Pincer Ligands. *Chem. Rev.* **2019**, *119*, 2681−2751. (g) Habraken, E. R. M.; Jupp, A. R.; Brands, M. B.; Nieger, M.; Ehlers, A. W.; Slootweg, J. C. Parallels between Metal-Ligand Cooperativity and Frustrated Lewis Pairs. *Eur. J. Inorg. Chem.* **2019**, *2019*, 2436−2442. (h) Higashi, T.; Kusumoto, S.; Nozaki, K. Cleavage of Si-H, B-H, and C-H Bonds by Metal-Ligand Cooperation. *Chem. Rev.* **2019**, *119*, 10393−10402. (i) Elsby, M. R.; Baker, R. T. Strategies and mechanisms of metal-ligand cooperativity in first-row transition metal complex catalysts. *Chem. Soc. Rev.* **2020**, *49*, 8933−8987. (j) Roy, B. C.; Ganguli, K.; Samim, S. A.; Kundu, S. Alkyl Phosphine Free, Metal-Ligand Cooperative Complex Catalyzed Alcohol Dehydrogenative Coupling Reactions. *Asian J. Org. Chem.* **2021**, *10*, 1218−1232.

(2) (a) Noyori, R.; Sandoval, C. A.; Muniz, K.; Ohkuma, T. Metal-ligand bifunctional catalysis for asymmetric hydrogenation. *Philos. Trans. R. Soc. London, Ser. A* **2005**, *363*, 901−912. (b) Muniz, K. Bifunctional metal-ligand catalysis: Hydrogenations and new reactions within the metal-(Di)amine scaffold. *Angew. Chem., Int. Ed.* **2005**, *44*, 6622−6627. (c) Ikariya, T.; Murata, K.; Noyori, R. Bifunctional transition metal-based molecular catalysts for asymmetric syntheses. *Org. Biomol. Chem.* **2006**, *4*, 393−406. (d) Gruetzmacher, H. Cooperating ligands in catalysis. *Angew. Chem., Int. Ed.* **2008**, *47*, 1814−1818. (e) Kuwata, S.; Ikariya, T. Quest for metal/NH bifunctional bioinspired catalysis in a dinuclear platform. *Dalton Trans.* **2010**, *39*, 2984−2992. (f) Morris, R. H. Exploiting Metal-Ligand Bifunctional Reactions in the Design of Iron Asymmetric Hydrogenation Catalysts. *Acc. Chem. Res.* **2015**, *48*, 1494−1502. (g) Vansuch, G. E.; Wu, C.-H.; Haja, D. K.; Blair, S. A.; Chica, B.; Johnson, M. K.; Adams, M. W. W.; Dyer, R. B. Metal-ligand cooperativity in the soluble hydrogenase-1 from Pyrococcus furiosus. *Chem. Sci.* **2020**, *11*, 8572−8581.

(3) (a) van der Vlugt, J. I.; Reek, J. N. H. Neutral Tridentate PNP Ligands and Their Hybrid Analogs: Versatile Non-Innocent Scaffolds for Homogeneous Catalysis. *Angew. Chem., Int. Ed.* **2009**, *48*, 8832−8846. (b) Goncalves, T. P.; Dutta, I.; Huang, K.-W. Aromaticity in catalysis: metal ligand cooperation via ligand dearomatization and rearomatization. *Chem. Commun.* **2021**, *57*, 3070−3082.

(4) (a) Devillard, M.; Bouhadir, G.; Bourissou, D. Cooperation between Transition Metals and Lewis Acids: A Way to Activate $H_2$ and H-E bonds. *Angew. Chem., Int. Ed.* **2015**, *54*, 730−732. (b) Owen, G. R. Functional group migrations between boron and metal centres within transition metal-borane and -boryl complexes and cleavage of H-H, E-H and E-E' bonds. *Chem. Commun.* **2016**, *52*, 10712−10726. (c) Tseng, K.-N. T.; Kampf, J. W.; Szymczak, N. K. Modular Attachment of Appended Boron Lewis Acids to a Ruthenium Pincer Catalyst: Metal-Ligand Cooperativity Enables Selective Alkyne Hydrogenation. *J. Am. Chem. Soc.* **2016**, *138*, 10378−10381. (d) Kiernicki, J. J.; Zeller, M.; Szymczak, N. K. Examining the Generality of Metal-Ligand Cooperativity Across a Series of First-Row Transition Metals: Capture, Bond Activation, and Stabilization. *Inorg. Chem.* **2020**, *59*, 9279−9286. (e) Hale, L. V. A.; Szymczak, N. K. Hydrogen Transfer Catalysis beyond the Primary Coordination Sphere. *ACS Catal.* **2018**, *8*, 6446−6461. (f) Karunananda, M. K.; Mankad, N. P. Cooperative Strategies for Catalytic Hydrogenation of Unsaturated Hydrocarbons. *ACS Catal.* **2017**, *7*, 6110−6119.

(5) (a) Dub, P. A.; Gordon, J. C. The mechanism of enantioselective ketone reduction with Noyori and Noyori-Ikariya bifunctional catalysts. *Dalton Trans.* **2016**, *45*, 6756−6781. (b) Dub, P. A.; Gordon, J. C. Metal-Ligand Bifunctional Catalysis: The "Accepted" Mechanism, the Issue of Concertedness, and the Function of the Ligand in Catalytic Cycles Involving Hydrogen Atoms. *ACS Catal.* **2017**, *7*, 6635−6655.

(6) (a) Greb, L.; Ebner, F.; Ginzburg, Y.; Sigmund, L. M. Element-Ligand Cooperativity with p-Block Elements. *Eur. J. Inorg. Chem.* **2020**, *2020*, 3030−3047. (b) Hasenbeck, M.; Gellrich, U. Boron-Ligand Cooperation: The Concept and Applications. *Chem. - Eur. J.* **2021**, *27*, 5615−5626.

(7) (a) Garrido-Barros, P.; Moonshiram, D.; Gil-Sepulcre, M.; Pelosin, P.; Gimbert-Surinach, C.; Benet-Buchholz, J.; Llobet, A. Redox Metal-Ligand Cooperativity Enables Robust and Efficient Water Oxidation Catalysis at Neutral pH with Macrocyclic Copper Complexes. *J. Am. Chem. Soc.* **2020**, *142*, 17434−17446. (b) Derrick, J. S.; Loipersberger, M.; Chatterjee, R.; Iovan, D. A.; Smith, P. T.; Chakarawet, K.; Yano, J.; Long, J. R.; Head-Gordon, M.; Chang, C. J. Metal-Ligand Cooperativity via Exchange Coupling Promotes Iron-Catalyzed Electrochemical $CO_2$ Reduction at Low Overpotentials. *J. Am. Chem. Soc.* **2020**, *142*, 20489−20501. (c) Wuttig, A.; Derrick, J. s.; Loipersberger, M.; Snider, A.; Head-Gordon, M.; Chang, C. j.; Toste, F. d. Controlled Single-Electron Transfer via Metal-Ligand Cooperativity Drives Divergent Nickel-Electrocatalyzed Radical Pathways. *J. Am. Chem. Soc.* **2021**, *143*, 6990−7001.

(8) Broere, D. L. J.; Plessius, R.; van der Vlugt, J. I. New avenues for ligand-mediated processes - expanding metal reactivity by the use of redox-active catechol, o-aminophenol and o-phenylenediamine ligands. *Chem. Soc. Rev.* **2015**, *44*, 6886−6915.
(9) (a) Fachinetti, G.; Floriani, C.; Mellini, M.; Merlino, S. Synthesis and x-ray crystal structure of the dimeric compound $[C_{16}H_{16}N_2O_2Ti(BH_3)_2]_2$, a dimer of NN'-ethylenebis[salicylidenaminato)titanium containing seven-co-ordinate titanium(IV) and amino-borane as donor groups. *J. Chem. Soc., Chem. Commun.* **1976**, 300−301. (b) Dell'Amico, G.; Marchetti, F.; Floriani, C. Peripheral electrophilic properties of dichloro[N,N'-ethylenebis(salicylideneiminato)]-titanium(IV): a route leading to a stable titanium-hydrogen-boron unit. *J. Chem. Soc., Dalton Trans.* **1982**, 2197−2202. (c) Stahl, T.; Muether, K.; Ohki, Y.; Tatsumi, K.; Oestreich, M. Catalytic Generation of Borenium Ions by Cooperative B-H Bond Activation: The Elusive Direct Electrophilic Borylation of Nitrogen Heterocycles with Pinacolborane. *J. Am. Chem. Soc.* **2013**, *135*, 10978−10981. (d) Anaby, A.; Butschke, B.; Ben-David, Y.; Shimon, L. J. W.; Leitus, G.; Feller, M.; Milstein, D. B-H Bond Cleavage via Metal-Ligand Cooperation by Dearomatized Ruthenium Pincer Complexes. *Organometallics* **2014**, *33*, 3716−3726. (e) Xu, Y.; Rettenmeier, C. A.; Plundrich, G. T.; Wadepohl, H.; Enders, M.; Gade, L. H. Borane-Bridged Ruthenium Complex Bearing a PNP Ligand: Synthesis and Structural Characterization. *Organometallics* **2015**, *34*, 5113−5118. (f) Bolano, T.; Esteruelas, M. A.; Gay, M. P.; Onate, E.; Pastor, I. M.; Yus, M. An Acyl-NHC Osmium Cooperative System: Coordination of Small Molecules and Heterolytic B-H and O-H Bond Activation. *Organometallics* **2015**, *34*, 3902−3908. (g) Schneck, F.; Assmann, M.; Balmer, M.; Harms, K.; Langer, R. Selective Hydrogenation of Amides to Amines and Alcohols Catalyzed by Improved Iron Pincer Complexes. *Organometallics* **2016**, *35*, 1931−1943. (h) Muller, F.; Trincado, M.; Pribanic, B.; Vogt, M.; Grutzmacher, H. Stable $BH_3$ adducts to rhodium amide bonds. *J. Organomet. Chem.* **2016**, *821*, 154−162. (i) Drover, M. W.; Schafer, L. L.; Love, J. A. Capturing HBCy2: Using N,O-Chelated Complexes of Rhodium(I) and Iridium(I) for Chemoselective Hydroboration. *Angew. Chem., Int. Ed.* **2016**, *55*, 3181−3186. (j) Drover, M. W.; Bowes, E. G.; Love, J. A.; Schafer, L. L. Accessing $\delta$-B-H Coordinated Complexes of Rh(I) and Ir(I) Using Mono- and Dihydroboranes: Cooperative Stabilization by a Phosphoramidate Coligand. *Organometallics* **2017**, *36*, 331−341. (k) Song, H.; Ye, K.; Geng, P.; Han, X.; Liao, R.; Tung, C.-H.; Wang, W. Activation of Epoxides by a Cooperative Iron-Thiolate Catalyst: Intermediacy of Ferrous Alkoxides in Catalytic Hydroboration. *ACS Catal.* **2017**, *7*, 7709−7717. (l) Zhang, J.; Liu, T.; Ma, Q.-Q.; Li, S.; Chen, X. A reaction of $[2,6\text{-}(^tBu_2PO)_2C_6H_3]NiSCH_2Ph$ with $BH_3$·THF: borane mediated C-S bond cleavage. *Dalton Trans.* **2018**, *47*, 6018−6024. (m) Scharf, L. T.; Weismann, J.; Feichtner, K.-S.; Lindl, F.; Gessner, V. H. Versatile Modes of Cooperative B-H Bond Activation Reactions in Ruthenium-Carbene Complexes: Addition, Ring-Opening and Insertion. *Chem. - Eur. J.* **2018**, *24*, 3439−3443. (n) Pang, M.; Wu, C.; Zhuang, X.; Zhang, F.; Su, M.; Tong, Q.; Tung, C.-H.; Wang, W. Addition of a B-H Bond across an Amido-Cobalt Bond: $Co^{II}$-H-Catalyzed Hydroboration of Olefins. *Organometallics* **2018**, *37*, 1462−1467. (o) Erken, C.; Kaithal, A.; Sen, S.; Weyhermüller, T.; Hölscher, M.; Werlé, C.; Leitner, W. Manganese-catalyzed hydroboration of carbon dioxide and other challenging carbonyl groups. *Nat. Commun.* **2018**, *9*, 4521. (p) Das, U. K.; Higman, C. S.; Gabidullin, B.; Hein, J. E.; Baker, R. T. Efficient and Selective Iron-Complex-Catalyzed Hydroboration of Aldehydes. *ACS Catal.* **2018**, *8*, 1076−1081. (q) Chen, J.-Y.; Liao, R.-Z. Mechanism and Regioselectivity of the Iron-Catalyzed Hydroboration of N-Heteroarenes: A Computational Study. *Organometallics* **2019**, *38*, 3267−3277. (r) Zhuang, X.; Chen, J.-Y.; Yang, Z.; Jia, M.; Wu, C.; Liao, R.-Z.; Tung, C.-H.; Wang, W. Sequential Transformation of Terminal Alkynes to 1,3-Dienes by a Cooperative Cobalt Pyridonate Catalyst. *Organometallics* **2019**, *38*, 3752−3759. (s) Elsby, M. R.; Baker, R. T. Cu(I)-SNS complexes for outer-sphere hydroboration and hydrosilylation of carbonyls. *Chem. Commun.* **2019**, *55*, 13574−13577. (t) Liu, J.; Chen, J.-Y.; Jia, M.; Ming, B.; Jia, J.; Liao, R.-Z.; Tung, C.-H.; Wang, W. Ni-O Cooperation versus Nickel(II) Hydride in Catalytic Hydroboration of N-Heteroarenes. *ACS Catal.* **2019**, *9*, 3849−3857. (u) Ghosh, C.; Kim, S.; Mena, M. R.; Kim, J.-H.; Pal, R.; Rock, C. L.; Groy, T. L.; Baik, M.-H.; Trovitch, R. J. Efficient Cobalt Catalyst for Ambient-Temperature Nitrile Dihydroboration, the Elucidation of a Chelate-Assisted Borylation Mechanism, and a New Synthetic Route to Amides. *J. Am. Chem. Soc.* **2019**, *141*, 15327−15337. (v) Hatzis, G. P.; Thomas, C. M. Metal-ligand cooperativity across two sites of a square planar iron(II) complex ligated by a tetradentate PNNP ligand. *Chem. Commun.* **2020**, *56*, 8611−8614. (w) MacNeil, C. S.; Hsiang, S.-J.; Hayes, P. G. Reversible dehydrogenation of a primary aryl borane. *Chem. Commun.* **2020**, *56*, 12323−12326. (x) Hou, S.-F.; Chen, J.-Y.; Xue, M.; Jia, M.; Zhai, X.; Liao, R.-Z.; Tung, C.-H.; Wang, W. Cooperative Molybdenum-Thiolate Reactivity for Transfer Hydrogenation of Nitriles. *ACS Catal.* **2020**, *10*, 380−390. (y) Zafar, M.; Ramalakshmi, R.; Ahmad, A.; Antharjanam, P. K. S.; Bontemps, S.; Sabo-Etienne, S.; Ghosh, S. Cooperative B-H and Si-H Bond Activations by $\kappa^2$-N,S-Chelated Ruthenium Borate Complexes. *Inorg. Chem.* **2021**, *60*, 1183−1194. (z) Higashi, T.; Kusumoto, S.; Nozaki, K. Umpolung of B-H Bonds by Metal-Ligand Cooperation with Cyclopentadienone Iridium Complexes. *Angew. Chem., Int. Ed.* **2021**, *60*, 2844−2848. (aa) Zhang, S.; Zhai, X.; Song, Y.; Feng, L.; Tung, C.-H.; Wang, W. Insertion of $BH_3$ into a Cobalt-Aryl Bond: Synthetic Routes to Arylborohydride and Borane-Amino Hydride Complexes. *Organometallics* **2021**, *40*, 1692−1698.
(10) Spielvogel, K. D.; Luna, J. A.; Loria, S. M.; Weisburn, L. P.; Stumme, N. C.; Ringenberg, M. R.; Durgaprasad, G.; Keith, J. M.; Shaw, S. K.; Daly, S. R. Influence of Multisite Metal-Ligand Cooperativity on the Redox Activity of Noninnocent $N_2S_2$ Ligands. *Inorg. Chem.* **2020**, *59*, 10845−10853.
(11) (a) Huff, C. A.; Sanford, M. S. Catalytic $CO_2$ Hydrogenation to Formate by a Ruthenium Pincer Complex. *ACS Catal.* **2013**, *3*, 2412−2416. (b) Filonenko, G. A.; Conley, M. P.; Coperet, C.; Lutz, M.; Hensen, E. J. M.; Pidko, E. A. The impact of Metal-Ligand Cooperation in Hydrogenation of Carbon Dioxide Catalyzed by Ruthenium PNP Pincer. *ACS Catal.* **2013**, *3*, 2522−2526. (c) Zhang, Y.; MacIntosh, A. D.; Wong, J. L.; Bielinski, E. A.; Williard, P. G.; Mercado, B. Q.; Hazari, N.; Bernskoetter, W. H. Iron Catalyzed $CO_2$ Hydrogenation to Formate Enhanced by Lewis Acid Co-Catalysts. *Chem. Sci.* **2015**, *6*, 4291−4299. (d) Filonenko, G. A.; Smykowski, D.; Szyja, B. M.; Li, G.; Szczygiel, J.; Hensen, E. J. M.; Pidko, E. A. Catalytic Hydrogenation of $CO_2$ to Formates by a Lutidine-Derived Ru-CNC Pincer Complex: Theoretical Insight into the Unrealized Potential. *ACS Catal.* **2015**, *5*, 1145−1154. (e) Bow, J.-P. J.; Boyle, P. D.; Blacquiere, J. M. Substrate-Mediated Deactivation of a Ru-$(P^tBu_2NBn_2)$ Cooperative Complex. *Eur. J. Inorg. Chem.* **2015**, *2015*, 4162−4166.
(12) Durgaprasad, G.; Luna, J. A.; Spielvogel, K. D.; Haas, C.; Shaw, S. K.; Daly, S. R. Ru(II) Complexes with a Chemical and Redox-Active $S_2N_2$ Ligand: Structures, Electrochemistry, and Metal-Ligand Cooperativity. *Organometallics* **2017**, *36*, 4020−4031.
(13) Sanford, M. S.; Love, J. A.; Grubbs, R. H. Mechanism and Activity of Ruthenium Olefin Metathesis Catalysts. *J. Am. Chem. Soc.* **2001**, *123*, 6543−6554.
(14) (a) Dub, P. A.; Scott, B. L.; Gordon, J. C. Air-Stable NNS (ENENES) Ligands and Their Well-Defined Ruthenium and Iridium Complexes for Molecular Catalysis. *Organometallics* **2015**, *34*, 4464−4479. (b) Sellmann, D.; Gottschalk-Gaudig, T.; Heinemann, F. W. Transition Metal Complexes with Sulfur Ligands. 130. Synthesis, Structure, and Reactivity of the Sulfur-Rich Ruthenium Hydride Complexes $[Ru(H)(PR_3)('S_{4'})]$- and the $\eta^2$-$H^2$ Complex $[Ru(H_2)(PCy_3)('S_{4'})]$ (R = Ph, $^i$Pr, Cy; '$S_{4'}^{2-}$ = 1,2-Bis((2-mercaptophenyl)-thio)ethane(2-)). *Inorg. Chem.* **1998**, *37*, 3982−3988. (c) Chirdon, D. N.; Kelley, S. P.; Hazari, N.; Bernskoetter, W. H. Comparative Coordination Chemistry of PNP and SNS Pincer Ruthenium Complexes. *Organometallics* **2021**, *40*, 4066.


https://doi.org/10.1021/acs.inorgchem.1c03014
*Inorg. Chem.* 2022, 61, 2391−2401

(15) Betley, T. A.; Qian, B. A.; Peters, J. C. Group VIII Coordination Chemistry of a Pincer-Type Bis(8-quinolinyl)amido Ligand. *Inorg. Chem.* **2008**, *47*, 11570−11582.
(16) The CV collected for **4** was similar to that for **3**. The only notable difference was that all of the features of **4** were shifted by ca. 0.1−0.2 V to more negative potentials due to the second $PPh_3$ ligand. See Figure S14 in the Supporting Information.
(17) Cramer, C. J. *Essentials of Computational Chemistry*, 2nd ed.; Wiley: Chichester, UK, 2004; pp 378−379.

## Recommended by ACS

**Molybdenum-Mediated Coupling of Carbon Monoxide to a C3 Product on a Single Metal Site**

Choon Heng Low, Theodor Agapie, *et al.*

MAY 09, 2022
INORGANIC CHEMISTRY

READ

**Polynuclear Iron(II) Pyridonates: Synthesis and Reactivity of Fe4 and Fe5 Clusters**

Andrey Fedulin, Axel Jacobi von Wangelin, *et al.*

APRIL 11, 2022
INORGANIC CHEMISTRY

READ

**Electronic Structure and Magnetic Properties of a Low-Spin CrII Complex: trans-[CrCl2(dmpe)2] (dmpe = 1,2-Bis(dimethylphosphino)ethane)**

Eva M. Zolnhofer, Joshua Telser, *et al.*

NOVEMBER 01, 2021
INORGANIC CHEMISTRY

READ

**Isolation and Characterization of a Highly Reducing Aqueous Chromium(II) Complex**

Scott E. Waters, Michael P. Marshak, *et al.*

JUNE 01, 2022
INORGANIC CHEMISTRY

READ

**Get More Suggestions >**



https://doi.org/10.1021/acs.inorgchem.1c03014
*Inorg. Chem.* 2022, 61, 2391−2401